Stability Analysis and Parameter Design of Virtual-Winding-Based Harmonic Current Controller for Permanent Magnet Synchronous Machines

Pingyue Song, *Student Member, IEEE*, Lijian Wu, *Senior Member, IEEE*, and Tao Wang, *Senior Member, IEEE*

***Abstract*—The multiple synchronous reference frame controller is a common method for harmonic control in permanent magnet synchronous machines (PMSMs), but its low-pass filter deteriorates the harmonic regulation dynamics and system stability. The virtual winding structure, as a novel alternative, can quickly separate each harmonic by vector space decoupling transformation. However, past studies have often assumed that the virtual winding structure does not affect closed-loop system performance or stability. This article constructs the equivalent transfer function of the virtual winding structure of a PMSM under resistance asymmetry. It is revealed that this structure is essentially a special filter. The stability of the closed-loop system is then studied in both continuous and discrete domains. The influence of speed and controller bandwidth on the stability boundary is analyzed. A parameter design method for the harmonic controller is proposed to optimize dynamic response while ensuring system stability. Finally, experimental results show that the theoretical and experimental stability boundaries have an error of less than 4%, validating the accuracy of the stability analysis and the effectiveness of the parameter design.**

***Index Terms*—Current control, multiple synchronous reference frame (MSRF), parameter design, stability analysis.**

I. Introduction

PERMANENT magnet synchronous machines (PMSMs) have seen widespread adoption over the past 20 years due to their high torque density, simple structure, and high efficiency [1]. Currently, PMSMs are utilized in various applications, including more-electric aircraft [2], marine propulsion systems [3], and electric vehicles [4]. However, nonideal factors such as impedance deviations, harmonics in the back electromotive force (EMF), and sensor inaccuracies introduce frequency disturbances in PMSM, leading to additional harmonics in traditional vector-controlled current regulators [5], [6], [7]. Harmonic currents not only increase total losses but also cause periodic torque ripples and vibration, which can significantly shorten the operational lifespan of the drive system [8], [9]. As a result, effective current harmonic regulation has become a critical area to fully exploit the performance potential of PMSM.

Extensive research has been conducted on the regulation of current harmonics. Model predictive control [10] and sliding mode control [11] can achieve rapid harmonic regulation. However, the process of selecting optimal space voltage vectors and the presence of nonlinear sliding mode surfaces often introduce high-frequency chattering in the current response. Harmonic current controllers based on various observers provide another solution, but their performance is often sensitive to parameter variations. Recently, hybrid harmonic current control techniques that combine observers with deadbeat controllers [12], [13] or repetitive controllers [14] have gained significant attention. These methods leverage the strengths of different controllers, offering enhanced parameter robustness and improved dynamic response. However, the increased designing complexity has significantly raised computational burden.

The proportional-integral-resonant (PIR) controllers and the multisynchronous reference frame (MSRF) controllers are two widely used harmonic current control techniques in engineering, valued for their simpler structures and ease of parameterization. The PIR controller, typically implemented in the *dq* coordinate, incorporates additional resonant terms alongside the original PI controller to provide extra gain for specific harmonic orders. This approach does not need the prefiltering of harmonics, allowing simultaneous regulation of both the fundamental and harmonic components. However, common issues exist in these methods, including potential deviations of the resonant frequency and the risk of instability and oscillations [15], [16], [17]. Using quasi-resonant terms rather than resonant terms can mitigate instability risks but may lead to increased steady-state error of each harmonic disturbance [18], [19].

Conversely, the MSRF controller involves both harmonic separation and harmonic regulation. This algorithm first extracts the fundamental and harmonic components from the measured currents through rotational transformations and low-pass filters (LPFs). The harmonics are then independently regulated in their respective synchronous reference frames using PI controllers, achieving zero steady-state error [20], [21], [22]. While harmonic separation helps minimize interference between different harmonic regulators, the use of LPFs limits the system's dynamic response. To overcome the limitations of LPFs, various studies have introduced alternative filtering structures. Yan et

Received 29 September 2024; revised 23 December 2024; accepted 19 January 2025. Date of current version 20 March 2025. This work was supported in part by the National Key Research and Development Program of China under Grant 2023YFB4202800 and in part by the National Science Fund for Distinguished Young Scholars under Grant 52225703. Recommended for publication by Associate Editor K.-B. Park. *(Corresponding author: Lijian Wu.)*

The authors are with the College of electrical engineering, Zhejiang University, Hangzhou City, Zhejiang Province CN 310027, China (e-mail: py_song@zju.edu.cn; ljw@zju.edu.cn; wangtaoee@zju.edu.cn).

Color versions of one or more figures in this article are available at https://doi.org/10.1109/TPEL.2025.3534840.

Digital Object Identifier 10.1109/TPEL.2025.3534840

al. [23], [24] proposed a virtual winding structure, converting a dual three-phase PMSM into a multi-three-phase configuration, which allows for the simultaneous separation and independent control of the –5th, +7th, –11th, and +13th harmonics. This method demonstrates a marked improvement in the dynamic performance of harmonic controllers compared to other MSRF enhancements. Lyu et al. [25] applied the virtual winding concept in *LC*-equipped PMSM drive systems to suppress back EMF harmonics. In [26], a generalized method for constructing virtual windings was proposed, enabling the decoupling and regulation of arbitrary harmonic currents, including even order harmonics and dc components.

However, most of the past research on virtual windings has focused on expanding the range of harmonic separation orders. Regarding the virtual winding structure itself, it is generally considered that, compared with the traditional LPFs, it does not affect the system's stability or dynamic response.

The structure of virtual windings differs from that of real multiphase PMSMs. To simplify the analysis, this article only takes the control of negative sequence first-order harmonics (–1st order) under resistance asymmetry as an example. The additional inductance asymmetry does not change the structure of the harmonic controller, nor does it affect the analytical framework of the proposed method. If the measured PMSM also exhibits inductance asymmetry, the modeling approach outlined in [33], [34], and [35] can be applied. A negative sequence harmonic controller based on virtual windings is constructed following the conclusions drawn in [26]. It is revealed that virtual windings are essentially a special type of filter. Based on this, the article derives the transfer function of the closed-loop system with virtual windings. The stability boundaries for the system in both continuous and discrete domains are presented. Experimental results confirm the theoretical stability boundaries within less than 4% error. Additionally, the article introduces a new parameter design method for harmonic controllers to achieve optimal dynamic performance. This design method not only ensures system stability compared to traditional approaches but also fully utilizes the high dynamic advantages of virtual windings. It should be noted that the proposed method is not limited to resistance asymmetry. It remains applicable in scenarios involving other types of harmonics, such as inverter dead-time effects, and back EMF harmonics. In such cases, the method can still assist in analyzing the stability of virtual windings and in designing the parameters of harmonic controllers.

This article reveals the equivalent filter for virtual windings for the first time, providing a more accurate evaluation of closed-loop system performance. Furthermore, the proposed parameter design method ensures the stability of any virtual-winding-based harmonic current controller, thereby advancing the practical application of this novel harmonic control approach.

The rest of this article is arranged as shown in Fig. 1. In Section II, PMSM, virtual winding, and closed-loop system are modeled, respectively. In Section III, the stability boundary of the closed-loop system with virtual winding structure is derived in the continuous and discrete domains, respectively. Besides, parameter sensitivity of the stability boundary is analyzed. In Section IV, the parameters of the negative sequence bandwidth ω_{cn} are adjusted according to the derived stability boundary, and the overall closed-loop control block diagram is obtained. In Section V, the steady and dynamic performance and stability of the proposed method are tested, and the computational burden of the virtual winding method is evaluated.

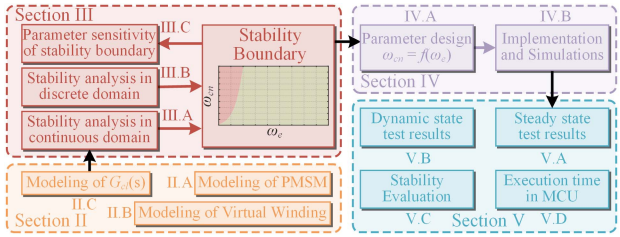

Fig. 1. Arrangement of the rest part of this article.

II. Modeling of the Closed-Loop Control System

A. Modeling of the PMSM Under Resistance Asymmetry

In the presence of resistance asymmetry in the PMSM drive system, the three-phase voltage u_{abc} can be represented as follows:

$$\begin{cases} u_a(t) = (R+\Delta R)i_a(t) + L_a\frac{\mathrm{d}}{\mathrm{d}t}i_a(t) + \frac{\mathrm{d}}{\mathrm{d}t}\psi_{fa}(t) \\ u_b(t) = Ri_b(t) + L_b\frac{\mathrm{d}}{\mathrm{d}t}i_b(t) + \frac{\mathrm{d}}{\mathrm{d}t}\psi_{fb}(t) \\ u_c(t) = Ri_c(t) + L_c\frac{\mathrm{d}}{\mathrm{d}t}i_c(t) + \frac{\mathrm{d}}{\mathrm{d}t}\psi_{fc}(t) \end{cases} \tag{1}$$

where $u_a(t)$, $u_b(t)$, and $u_c(t)$ are the stator voltages in the *abc* frame, $i_a(t)$, $i_b(t)$, and $i_c(t)$ are the stator currents in the *abc* frame. L_a, L_b, and L_c; are the stator inductances in the *abc* frame, ψ_{fa} (*t*), $\psi_{fb}(t)$, and $\psi_{fc}(t)$ are the permanent magnet flux linkages in the *abc* frame. *R* is the stator resistance, and ΔR is the additional asymmetrical resistance in phase A.

If leakage inductances and the magnetic saturation effects are neglected, (1) can be converted into the *dq* axes [27], [28] as follows:

$$\begin{cases} u_d(t) = R'i_d(t) + L_d\frac{\mathrm{d}}{\mathrm{d}t}i_d(t) \\ \qquad -\omega_e L_q i_q(t) \underbrace{+K_{\Delta R}\,|i_{dq}|\cos(-2\theta_e)}_{u_{dn2}(t)} \\ u_q(t) = R'i_q(t) + L_q\frac{\mathrm{d}}{\mathrm{d}t}i_q(t) + \omega_e L_d i_d(t) \\ \qquad +\omega_e\psi_f \underbrace{-K_{\Delta R}\,|i_{dq}|\sin(-2\theta_e)}_{u_{qn2}(t)} \end{cases} \tag{2}$$

where $u_d(t)$ and $u_q(t)$ are the stator voltages in *dq* axes, $i_d(t)$ and $i_q(t)$ are the stator currents in *dq* axes. L_d and L_q are the inductances in *dq* axes, ψ_f is the amplitude of the permanent magnet flux linkage, ω_e is the electrical angular velocity of the PMSM, θ_e is the electrical angular, $R' = R+\Delta R/3$ represents the equivalent average resistance of the PMSM under asymmetry, $|i_{dq}| = \sqrt{i_d^2 + i_q^2}$ is the amplitude of the currents vector in *dq* axes, $K_{\Delta R}$ is a constant coefficient related to ΔR and can be

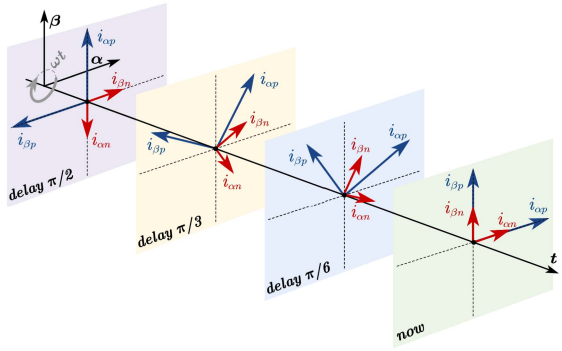

Fig. 2. Schematic diagram of virtual winding structure to realize harmonic current separation.

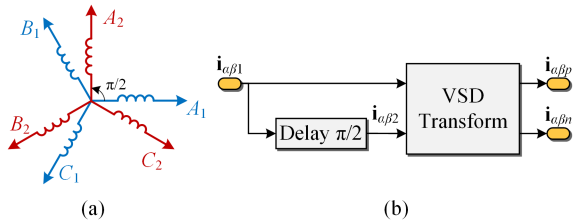

Fig. 3. Constructed virtual windings and VSD transformation. (a) Structure of virtual winding. (b) Vector space decoupling transformation based on virtual windings.

expressed as follows:

$$K_{\Delta R} = \sqrt{\left(\frac{\Delta R}{3}\right)^2 - \frac{\Delta R}{3}}. \tag{3}$$

It can be observed from (2) that the asymmetrical resistance introduces the –2nd harmonic voltage disturbances $u_{dn2}(t)$ and $u_{qn2}(t)$ in the stator voltages. Therefore, if the output voltage commands of the current controllers are constant in *dq* frame, the disturbances $u_{dn2}(t)$ and $u_{qn2}(t)$ will inevitably induce fluctuations in $i_d(t)$ and $i_q(t)$. The electromagnetic torque generated by the PMSM can be expressed as follows [29]:

$$T_e = \frac{3}{2} p_n i_q [i_d(L_d - L_q) + \psi_f] \tag{4}$$

where p_n represents the number of pole pairs. According to (2) and (4), the fluctuations in $i_d(t)$ and $i_q(t)$ caused by resistance asymmetry will result in torque ripple in the output torque T_e. To mitigate these torque pulsations, the current controller needs to generate additional harmonic voltages to counteract the disturbances introduced by u_{dn2} and u_{qn2}. To achieve this, a negative-sequence current controller must be constructed to eliminate the negative-sequence harmonic currents.

It is worth noting that, although the above analysis only considers the asymmetrical resistance in phase A, the analysis results remain valid when resistance asymmetry exists in other phases. This means that negative-sequence disturbances $u_{dn2}(t)$ and $u_{qn2}(t)$ still exist, and the amplitude $K_{\Delta R}$ and the initial phase of $u_{dn2}(t)$ and $u_{qn2}(t)$ will vary accordingly [28].

B. Modeling and Principle of the Virtual Winding Structure

According to the previous section, a negative-sequence harmonic current controller should be designed to eliminated the harmonic currents. In this article, a set of virtual windings is constructed to separate the positive and the –1st harmonic currents simultaneously. The virtual windings can be obtained through a fixed-angle delay operation. In actual controllers, the delay operation can be performed by storing past sampled currents in real time and retrieving them using a lookup table.

Fig. 2 illustrates the diagram of harmonic separation through a virtual winding structure, where $i_\alpha = i_{\alpha p} + i_{\alpha n}$, $i_\beta = i_{\beta p} + i_{\beta n}$ represent the sampled currents in $\alpha\beta$ axes, where the subscripts "*p*" and "*n*" refer to the positive and negative sequence components, respectively. The green plane represents the current vector plane at this moment. The cyan, yellow, and purple planes represent the current vector plane before this moment with $\pi/6$, $\pi/3$, and $\pi/2$ electrical angle, respectively. If the PMSM operates in a steady state, the amplitudes of each harmonic currents remain constant. As the delay angle increases, $i_{\alpha p}$ and $i_{\beta p}$ rotates counterclockwise, while $i_{\alpha n}$ and $i_{\beta n}$ rotates clockwise. When the delay angle reaches $\pi/2$, the positive and negative sequence currents counteract each other, which can be expressed as follows:

$$\begin{cases} i_\alpha = i_{\alpha p} + i_{\alpha n} & i_\alpha e^{-j\pi/2} = i_{\alpha p} - i_{\alpha n} \\ i_\beta = i_{\beta p} + i_{\beta n} & i_\beta e^{-j\pi/2} = i_{\beta p} - i_{\beta n}. \end{cases} \tag{5}$$

Thus, harmonic current separation can be achieved by solving (5). In general, to simultaneously separate the fundamental and the *h*th harmonic currents, the required delay angle delay λ must satisfy [26]

$$\lambda = \left| \frac{\pi}{1-h} \right|. \tag{6}$$

In this article, the –1st harmonic current need to be separated, i.e., $h = -1$. Therefore, the required delay angle λ is $\pi/2$. Then, the required delay time δ for the virtual windings can be expressed as follows:

$$\delta = \frac{1}{4}\frac{2\pi}{\omega_e} = \frac{\pi}{2\omega_e}. \tag{7}$$

Fig. 3(a) presents the schematic diagram of the original winding and the constructed virtual winding in this article. The blue windings are the actual windings of the three-phase PMSM, while the red windings are the constructed virtual windings. The virtual windings need to be delayed by $\pi/2$ to the actual windings at all ω_e.

Additionally, to achieve current harmonic separation, the VSD decoupling transformation should be applied to both the original and virtual currents. To reduce storage requirements, the currents in the *abc* frame can be transformed into the $\alpha\beta$ frame before the delay operation. The VSD decoupling transformation to separate the fundamental and –1st harmonic components can be expressed as follows:

$$\begin{bmatrix} \mathbf{i}_{\alpha\beta p} \\ \mathbf{i}_{\alpha\beta n} \end{bmatrix} = \frac{2}{4} \begin{bmatrix} \mathbf{T}_{\alpha\beta}(0) & \mathbf{T}_{\alpha\beta}(-\pi/2) \\ \mathbf{T}_{\alpha\beta}(0) & \mathbf{T}_{\alpha\beta}(\pi/2) \end{bmatrix} \begin{bmatrix} \mathbf{i}_{\alpha\beta 1} \\ \mathbf{i}_{\alpha\beta 2} \end{bmatrix} \tag{8}$$

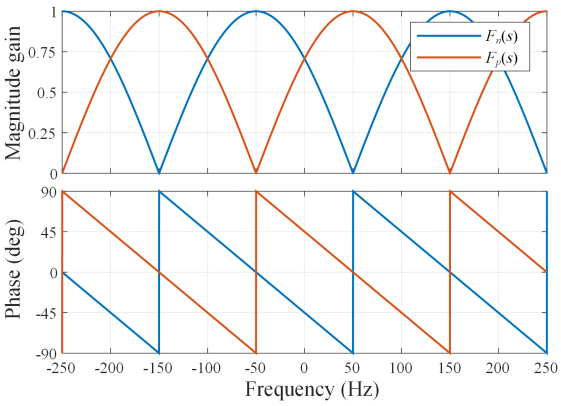

Fig. 4. Bode diagram of the equivalent filters $F_p(s)$ and $F_n(s)$ based on virtual windings and VSD.

where $\mathbf{i}_{\alpha\beta1} = [i_{\alpha1}, i_{\beta1}]^{\mathrm{T}}$ is the actual current vector in $\alpha\beta$ axes, $\mathbf{i}_{\alpha\beta2} = [i_{\alpha2}, i_{\beta2}]^{\mathrm{T}}$ is the virtual current vector in $\alpha\beta$ axes, $\mathbf{i}_{\alpha\beta p} = [i_{\alpha p}, i_{\beta p}]^{\mathrm{T}}$, and $\mathbf{i}_{\alpha\beta n} = [i_{\alpha n}, i_{\beta n}]^{\mathrm{T}}$ are the positive and negative components after decoupling transformation. The coefficient 2/4 represents the equal amplitude transformation. The transformation submatrix $\mathbf{T}_{\alpha\beta}(\theta)$ can be expressed as follows:

$$\mathbf{T}_{\alpha\beta}(\theta) = \begin{bmatrix} \cos(\theta) & \cos(\theta - \pi/2) \\ \sin(-\theta) & \sin(\pi/2 - \theta) \end{bmatrix}. \tag{9}$$

The schematic diagram of harmonic separation based on the virtual winding and VSD decoupling transformation is shown in Fig. 3(b). To further reveal the essence of the virtual winding structure, the delay operation is re-expressed in the frequency domain, that is

$$i_{\alpha2}(s) = e^{-s\delta} i_{\alpha1}(s), \quad i_{\beta2}(s) = e^{-s\delta} i_{\beta1}(s) \tag{10}$$

where s is the Laplace operator. For simplicity, (s) is omitted in the subsequent analysis. Equation (8) can be converted into the form of complex vectors, which can be expressed as follows:

$$\begin{cases} \boldsymbol{i}_{\alpha\beta p} = F_p(s)\boldsymbol{i}_{\alpha\beta1} = \frac{e^{s\delta} + e^{j\pi/2}}{2e^{s\delta}} \boldsymbol{i}_{\alpha\beta1} \\ \boldsymbol{i}_{\alpha\beta n} = F_n(s)\boldsymbol{i}_{\alpha\beta1} = \frac{e^{s\delta} + e^{-j\pi/2}}{2e^{s\delta}} \boldsymbol{i}_{\alpha\beta1} \end{cases} \tag{11}$$

where $\boldsymbol{i}_{\alpha\beta} = i_\alpha + ji_\beta$, $\boldsymbol{i}_{\alpha\beta p} = i_{\alpha p} + ji_{\beta p}$, $\boldsymbol{i}_{\alpha\beta n} = i_{\alpha n} + ji_{\beta n}$ represents the complex vector of the original currents, positive sequence currents, and negative sequence currents. $F_p(s)$ and $F_n(s)$ are the equivalent transfer functions from $\boldsymbol{i}_{\alpha\beta}$ to $\boldsymbol{i}_{\alpha\beta p}$ and $\boldsymbol{i}_{\alpha\beta n}$, respectively. To clearly show their characteristics, the Bode diagram of the two equivalent transfer functions of $F_p(s)$ and $F_n(s)$ is presented, as shown in Fig. 4. It can be observed from Fig. 4 that $F_p(s)$ can realize the unit gain extraction of positive sequence currents and the elimination of negative sequence currents, while $F_n(s)$ can realize the unit gain extraction of negative sequence currents and the elimination of positive sequence currents. Therefore, $F_p(s)$ and $F_n(s)$ can be regarded as two special filters. Similarly, if the extracted harmonic components are –5th and +7th harmonics, such as the virtual winding constructed in [23], using the above analysis method, several similar filters can be obtained. Therefore, the VSD transformation based on a virtual winding structure is essentially a set of special complex coefficient filters with fixed-angle delay.

C. Modeling of the Closed-Loop Control System

If the tested motor is a surface-mounted PMSM (SPMSM), then L_d and L_q are equal, denoted as L. Furthermore, by applying the rotational transformation to (2) and expressing it in the form of a complex vector, the model of the PMSM in the $\alpha\beta$ frame under resistance asymmetry can be obtained as follows:

$$\begin{aligned} \boldsymbol{i}_{\alpha\beta} &= \frac{1}{sL + R'} \left(\boldsymbol{u}_{\alpha\beta} - \boldsymbol{e}_{\alpha\beta} + \boldsymbol{d}_{\alpha\beta n} \right) \\ &= P(s) \left(\boldsymbol{u}_{\alpha\beta} - \boldsymbol{e}_{\alpha\beta} + \boldsymbol{d}_{\alpha\beta n} \right) \end{aligned} \tag{12}$$

where $\boldsymbol{e}_{\alpha\beta}$ represents the back EMF complex vector in $\alpha\beta$ axes, $\boldsymbol{u}_{\alpha\beta}$ represents the total output voltage complex vector of the inverter, R' and L are the equivalent stator resistance and stator inductance of the SPMSM, $\boldsymbol{d}_{\alpha\beta n}$ represents the lumped –1st harmonic voltage disturbance caused by the asymmetrical resistance. $P(s)$ represents the equivalent transfer function of the SPMSM.

To achieve zero steady-state error, the automatic current regulator (ACR) usually uses a proportional-integral (PI) controller. Furthermore, to improve the dynamics of current loop regulation, a complex vector PI controller [30] can be utilized. The transfer function of the complex vector PI controller in $\alpha\beta$ axes can be expressed as follows:

$$G_p(s) = \frac{sK_{pp} + K_{ip}}{s - j\omega_e} \tag{13}$$

where $K_{pp} = \omega_{cp} L_e$ and $K_{ip} = \omega_{cp} R'_e$ represent the proportional and integral parameters of the positive-sequence currents, respectively, L_e and R'_e are the estimated inductance and resistance, and ω_{cp} represents the bandwidth of the positive-sequence ACR (ACRp).

Since the negative sequence currents are usually smaller than the positive sequence currents, for simplicity, the traditional PI controller is used for negative-sequence ACR (ACRn) in this article. The transfer function of ACRn in the $\alpha\beta$ axes can be expressed as follows:

$$G_n(s) = K_{pn} + \frac{K_{in}}{s + j\omega_e} \tag{14}$$

where $K_{pn} = \omega_{cn} L_e$ and $K_{in} = \omega_{cn} R'_e$ represent the proportional and integral parameters, respectively, and ω_{cn} represents the bandwidth of the ACRn.

Fig. 5 shows the block diagram of the closed-loop control system in the $\alpha\beta$ axes virtual-winding-based harmonic current controller and the proposed parameter design method, where $\boldsymbol{u}_{\alpha\beta p}$ and $\boldsymbol{u}_{\alpha\beta n}$ represent the positive and negative sequence output voltage vector of ACRp and ACRn, respectively. The blue arrow $\boldsymbol{d}_{\alpha\beta n}$ denotes the equivalent negative sequence disturbance voltage caused by resistance asymmetry. $G_p(s)$ and $G_n(s)$ represent the transfer function of ACRp and ACRn in the $\alpha\beta$ axes, respectively. The cyan region represents the equivalent filter of the VSD and the virtual winding. $\boldsymbol{i}_{\alpha\beta pr}$ and $\boldsymbol{i}_{\alpha\beta nr}$ are the command values of positive and negative sequence currents,

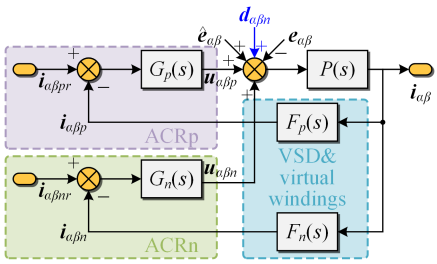

Fig. 5. Block diagram of the closed-loop system with virtual-winding-based harmonic current controller and the proposed parameter design method in the $\alpha\beta$ frame.

$\boldsymbol{i}_{\alpha\beta p}$ and $\boldsymbol{i}_{\alpha\beta n}$ are the separated positive and negative sequence currents, and $\hat{\boldsymbol{e}}_{\alpha\beta}$ denotes the estimated value of back EMF. The output current $\boldsymbol{i}_{\alpha\beta}$ of the system can be expressed as follows:

$$\begin{aligned}\boldsymbol{i}_{\alpha\beta} = {} & G_{ipr}(s)\boldsymbol{i}_{\alpha\beta pr} + G_{inr}(s)\boldsymbol{i}_{\alpha\beta nr} \\ & + G_{iu}(s)\left(\hat{\boldsymbol{e}}_{\alpha\beta} - \boldsymbol{e}_{\alpha\beta} + \boldsymbol{d}_{\alpha\beta n}\right)\end{aligned} \tag{15}$$

where $G_{ipr}(s)$, $G_{inr}(s)$, and $G_{iu}(s)$ are the equivalent closed-loop transfer functions from $\boldsymbol{i}_{\alpha\beta pr}$, $\boldsymbol{i}_{\alpha\beta nr}$, ($\hat{\boldsymbol{e}}_{\alpha\beta}$-$\boldsymbol{e}_{\alpha\beta}$ + $\boldsymbol{d}_{\alpha\beta n}$) to the output current $\boldsymbol{i}_{\alpha\beta}$, respectively. According to Fig. 5, the transfer function of $G_{ipr}(s)$, $G_{inr}(s)$, and $G_{iu}(s)$ can be deduced as follows:

$$\begin{cases} G_{inr}(s) = \frac{G_n(s)P(s)}{1+F_n(s)G_n(s)P(s)+F_p(s)G_p(s)P(s)} \\ G_{ipr}(s) = \frac{G_p(s)P(s)}{1+F_n(s)G_n(s)P(s)+F_p(s)G_p(s)P(s)} \\ G_{iu}(s) = \frac{P(s)}{1+F_n(s)G_n(s)P(s)+F_p(s)G_p(s)P(s)}. \end{cases} \tag{16}$$

If the estimation of the back EMF is accurate, that is, $\boldsymbol{e}_{\alpha\beta}$- $\hat{\boldsymbol{e}}_{\alpha\beta}$ $\approx$ 0, the fundamental back EMF hardly affects the dynamics of the output current, so only the influence of the $\boldsymbol{d}_{\alpha\beta n}$ perturbation caused by the asymmetry exists.

III. Stability Analysis of Virtual Winding Structure

A. Stability Analysis in Continuous Domain

To analyze the stability of the closed-loop control system based on virtual winding, according to the classical control theory, the characteristic roots of the closed-loop system need to be located on the left side of the complex plane, that is, there is no pole with a positive real part. Assume that the estimated impedance are identical to the actual values, i.e., $L_e = L$, and $R'_e = R'$. According to (16), the characteristic equations of the three closed-loop transfer functions $G_{ipr}(s)$, $G_{inr}(s)$, and $G_{iu}(s)$ can be expressed as follows:

$$E_c(s) = a_3 s^2 + a_2 s^2 + a_1 s + a_0 \tag{17}$$

where $E_c(s)$ denotes the characteristic equation of the closed-loop system, and a_3, a_2, a_1, and a_0 denote the coefficients of each term in (17), which is shown in the Appendix.

It can be seen from (26) that the delay operation leads to $e^{-s\delta}$ in $E_c(s)$, which converts the system into an infinite-dimensional nonlinear system and cannot be analyzed by classical control theory. To address this problem, the Pade approximation is utilized to linearize $e^{-s\delta}$ in this article [31]. The Pade approximation of $e^{-s\delta}$ can be expressed as follows:

$$e^{-s\delta} \approx \frac{\left(1 - \frac{\delta}{2n}s\right)^n}{\left(1 + \frac{\delta}{2n}s\right)^n} \tag{18}$$

where n denotes the order of the Pade approximation. When $n = 1$, the 1st Pade approximation of $e^{-s\delta}$ can be expressed as follows:

$$e^{-s\delta} \approx \frac{2 - \delta s}{2 + \delta s}. \tag{19}$$

However, the Pade approximation can only maintain the frequency domain characteristics near $s = 0$, which cannot be directly applied to (26). Considering that the frequencies of ω_e and $-\omega_e$ are the desired frequencies of $F_p(s)$ and $F_n(s)$, respectively, the shift transform (equivalent to the rotational transform in the time domain) can be implemented. Then, the Pade approximation in (19) can be used. The equivalent filters of virtual winding after Pade approximation can be derived as follows:

$$\begin{aligned} F_p(s) &= \frac{1}{2}\left(1 + e^{j\pi/2}e^{-\delta s}\right) = \frac{1}{2}\left(1 + e^{j(\pi/2 - \delta\omega_e)}e^{-\delta(s - j\omega_e)}\right) \\ &\approx \frac{1}{2}\left(1 + e^{j(\pi/2 - \delta\omega_e)}\frac{2 - \delta\left(s - j\omega_e\right)}{2 + \delta\left(s - j\omega_e\right)}\right) \end{aligned} \tag{20}$$

$$\begin{aligned} F_n(s) &= \frac{1}{2}\left(1 + e^{j\pi/2}e^{-\delta s}\right) = \frac{1}{2}\left(1 + e^{j(-\pi/2 + \delta\omega_e)}e^{-\delta(s + j\omega_e)}\right) \\ &\approx \frac{1}{2}\left(1 + e^{j(-\pi/2 + \delta\omega_e)}\frac{2 - \delta\left(s + j\omega_e\right)}{2 + \delta\left(s + j\omega_e\right)}\right). \end{aligned} \tag{21}$$

Combining (21), (20), (26), the characteristic equation of the closed-loop system after 1st Pade approximation can be obtained, which can be expressed as follows:

$$E_{ce1}(s) = b_5 s^5 + b_4 s^4 + b_3 s^3 + b_2 s^2 + b_1 s + b_0 \tag{22}$$

where $E_{ce1}(s)$ denotes the approximate characteristic equation. b_5, b_4, b_3, b_2, b_1, b_0 represent the coefficients of $E_{ce1}(s)$, which are shown as in the Appendix.

Coefficients b_5–b_0 in (27)–(32) demonstrate that the Pade approximation converts the system into a polynomial form, thereby increasing the maximum order of the $E_{ce1}(s)$. Although higher order Pade approximations better approximate the original system's characteristics, they also result in a higher order of the closed-loop system.

To verify the influence of Pade approximation on the characteristics of the closed-loop system, the Bode diagram of $F_p(s)$, $F_n(s)$, and the closed-loop transfer function before and after Pade approximation are presented, which is shown in Fig. 6. The subscript e represents the results after approximation. It can be seen from Fig. 6 that $F_{pe}(s)$ and $F_{ne}(s)$ retain the characteristics near $\pm\omega_e$. And the frequency domain curves of $G_{ipre}(s)$ and $G_{inre}(s)$ after Pade approximation are coincident with the original transfer function, which indicates that Pade approximation greatly simplifies the analysis process without significantly affecting the characteristics of the closed-loop system.

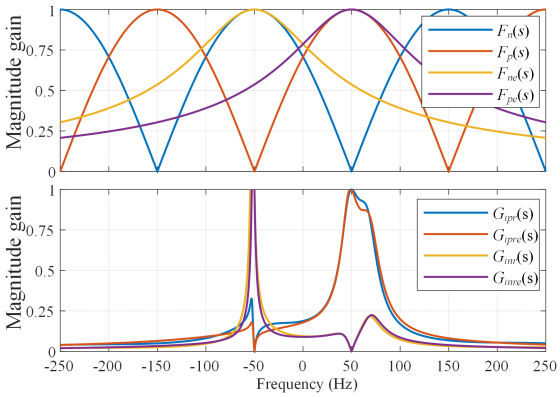

Fig. 6. Bode diagram of the equivalent filters and closed-loop transfer function before and after Pade approximation, where $\omega_e = 50\pi$ rad/s, $\omega_{cp} = 20\pi$, $\omega_{cn} = 10\pi$.

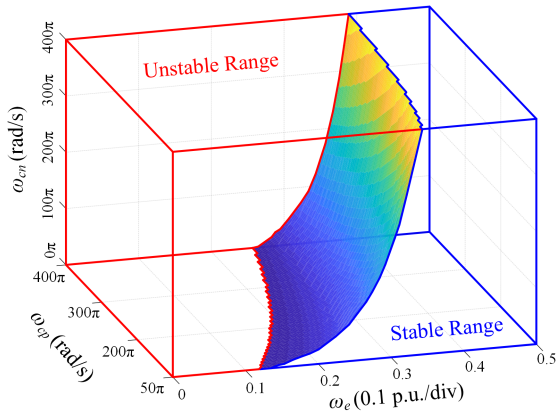

Fig. 7. Stable region of the closed loop system under different of ω_{cp}, ω_{cn}, and ω_e in continuous domain.

TABLE I
PARAMETERS OF THE TEST PMSM

Parameter	Value
Rated speed	1000 rpm
Rated current	5 A
Pole pairs	4
Stator inductance	4 mH
Stator resistance	1 Ω

Considering ω_{cp}, ω_{cn}, and ω_e are typically bounded, the coefficients b_5 to b_0 can be determined numerically. By calculating the roots of $E_{ce1}(s)$ with a fixed step size, the stability of the closed-loop system can be analyzed. This analysis allows for the determination of the feasible region that ensures system stability.

Fig. 7 is the distribution of the stable and unstable region of the closed-loop system under different combinations of ω_{cp}, $\omega_{cn,}$ and ω_e, where the rated speed and pole pairs are the same as the tested prototype in Table I. The two-dimensional surface represents the maximum negative sequence bandwidth ω_{cn} that can be achieved to ensure stability, which divides the whole space into two ranges. The blue part is the stable subspace and the red part is the unstable subspace.

Additionally, it is observed that as ω_{cp} decreases, ω_e increases, which results in a larger stable subspace. Therefore, to ensure stable operation, the chosen values of ω_{cp} and ω_{cn} must be confined within the stable subspace corresponding to each ω_e.

B. Stability Analysis in the Discrete Domain

The Pade approximation offers an effective solution for the equivalent of $e^{-s\delta}$. The second alternative solution is to directly discretize the system with the help of $z = e^{sTs}$. The transfer function can be converted into the discrete form with the variable z. and the discrete form of the equivalent filter can be derived as follows:

$$F_p(z) = \frac{z^N + e^{j\pi/2}}{2z^N} \quad F_n(z) = \frac{z^N + e^{-j\pi/2}}{2z^N} \tag{23}$$

where N represents the number of switching periods for the delay. Considering the delay angle is an integer multiple of the switching period, N can be expressed as follows:

$$N = \left[\frac{\pi}{2\omega_e T_s}\right] \tag{24}$$

where [] denotes the rounding of the calculated results and N determines the highest order of the discrete transfer function. Thus, (24) indicates that the maximum order of the closed-loop system's delay depends on ω_e, a lower ω_e results in a higher order of the entire discrete transfer function. In this article, the Tustin transformation is employed to discretize the closed-loop system, accounting for the computational delay as $G_d(z) = e^{-j\omega eTs} z^{-1}$ [32]. The derived discrete closed-loop transfer function from the positive sequence reference input $\boldsymbol{i}_{\alpha\beta pr}$ to output $\boldsymbol{i}_{\alpha\beta}$ can be represented as follows:

$$G_{ipr}(z) = \frac{G_p(z)P(z)G_d(z)}{1 + F_n(z)G_n(z)P(z)G_d(z) + F_p(z)G_p(z)P(z)G_d(z)}. \tag{25}$$

The characteristic equations of the other two closed-loop transfer functions are identical to $G_{ipr}(z)$ and are therefore omitted. Due to the complexity of the discrete transfer function expressions, they are not included in this article to save space. By solving the roots of the denominator in (25), the root loci of the closed-loop system for different ω_e can be obtained during ω_{cn} increases, as shown in Fig. 8. It reveals several interesting conclusions. First, as ω_e increases, the number of roots decreases, consistent with the properties of (24). Additionally, among the roots near (10), one root always moves further from the unit circle as ω_{cn} increases, leading the closed-loop system to transition from stability to instability. This observation aligns with the stability region distribution shown in Fig. 7.

Fig. 9 shows the maximum distance from the characteristic roots to the origin under different ω_{cn} and ω_e, which can be seen as an indicator for stability. The bandwidth ω_{cp} is set to 100π. Typically, ω_{cn} is smaller than ω_{cp}, thus, the vertical axis represents the ratio of ω_{cn} to ω_{cp}, with a maximum value of 1. Contour lines highlight cases where this maximum distance from roots to (00) is the same. The distance of 1 indicates the system's stability boundary. The green area denotes the system is stable, while the red area denotes instability. Fig. 9 can be

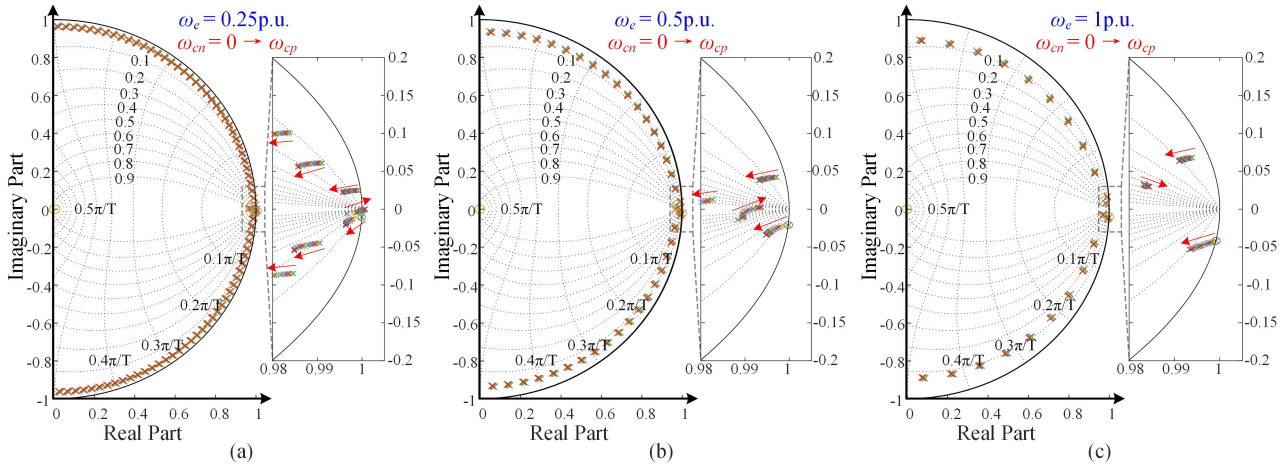

Fig. 8. Root locus of the discrete system at different speed ω_e during the increasing of ω_{cn}. (a) $\omega_e = 0.25$ p.u., ω_{cn} increases from 0 to ω_{cp}. (b) $\omega_e = 0.5$ p.u., ω_{cn} increases from 0 to ω_{cp}. (c) $\omega_e = 1$ p.u., ω_{cn} increases from 0 to ω_{cp}.

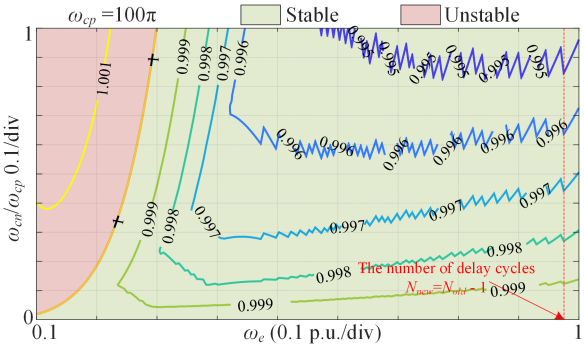

Fig. 9. Stable region of the closed-loop system under different ω_{cn} and ω_e in discrete domain, where ω_{cp} =100π, the contour from 0.995 to 1.001 represents the maximum distance from the closed-loop roots to origin (00).

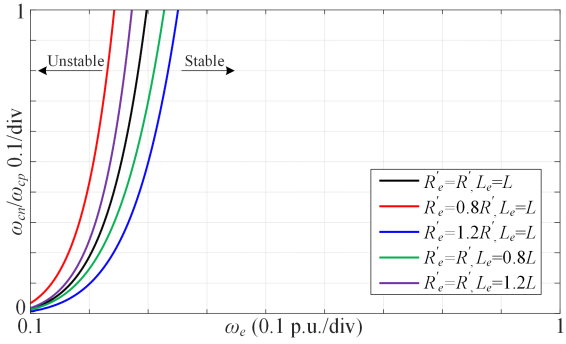

Fig. 10. Comparison of the analyzed stability boundaries with and without parameter mismatch.

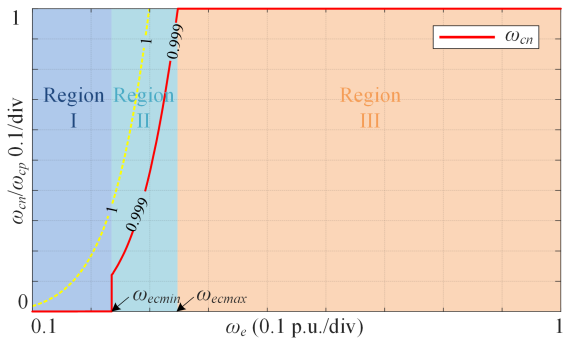

Fig. 11. Parameter design of the bandwidth of the negative sequence ACR ω_{cn}, where $\omega_{cp} = 100\pi$.

regarded as a cross-section of the stable and unstable subspace in Fig. 7 when $\omega_{cp} = 100\pi$.

It is worth noting that the minimum ω_e in Fig. 9 is set to 0.1 p.u. This is mainly because, when ω_e is small, the order of the discrete polynomial increases significantly, resulting in a substantial rise in computational burden. For example, when $\omega_e = 0.1$ p.u., according to the parameters in Table I and (24), it can be calculated that $N = 375$. This implies that the characteristic equation has at least 375 complex roots, which brings significant challenges for the numerical calculation.

In addition, it can be observed from Fig. 9 that the contour line with values less than 1 have multiple turns. This is because N decreases during the increase of ω_e, that is, the order of the system and the total number of characteristic roots decrease at a specific frequency point (red dotted line), which result in different distribution of characteristic roots and repeated turning of contour lines.

C. Parameter Sensitivity of the Stability Boundary

Fig. 10 compares the stability boundaries obtained using the above analysis method with and without parameter mismatch. As shown in Fig. 10, deviation between the estimated and actual parameters cause variation in the closed-loop system's stability boundary. Specifically, overestimating the R' or underestimating the L leads to a contraction of the stability region, and vice versa. Despite these variations, the bandwidth ω_{cn} can still be designed in three segments as depicted in Fig. 11, indicating the proposed parameter design method is still applicable under parameter mismatch. It should be noted that, in practical applications, to

maintain sufficient stability margins under parameter deviation, ω_{cn} should be determined under the worst-case scenario, i.e., the stability region is minimized caused by the parameter mismatch.

IV. Parameter Design and Implementation

A. Parameter Design

Fig. 9 indicates that using a constant ω_{cn} could lead to instability at low speeds or failure to fully utilize the high dynamic advantage of the virtual winding at high speeds. To address this issue, ω_{cn} should be adjusted in real-time to achieve dynamic optimization of ACRn while maintaining the closed-loop system's stability. One simple approach is change ω_{cn} using a lookup table under different ω_e. It is worth noting that, for simplicity, this article uses a lookup table method to achieve parameterization of ω_{cn}. However, adjusting ω_{cn} based on a lookup table of ω_e is not the only tuning method. Analytical parameterization can be realized by modeling the system as a 2x2 orthogonal multiple-input, multiple-output (MIMO) system [37]. A detailed parameter design is suggested as a direction for future research.

To ensure the closed-loop system has enough stability margin, this article requires that the maximum distance of the characteristic roots from the origin does not exceed 0.999. Consequently, ω_{cn} can be designed as the red line shown in Fig. 11, where ω_{ecmin} represents the minimum critical ω_e required to meet this criterion, and ω_{ecmax} represents the maximum critical ω_e when $\omega_{cn} = \omega_{cp}$. These two boundaries divide the entire area into three regions: Region I: $\omega_e < \omega_{ecmin}$, as indicated by the blue region in Fig. 11. To prevent potential instability, set $\omega_{cn} = 0$ and disable the ACRn. Region II: $\omega_{ecmin} \le \omega_e \le \omega_{ecmax}$, as indicated by the cyan region. To optimize the dynamics of ACRn, set ω_{cn} such that the maximum magnitude of the characteristic roots equals 0.999. Region III: $\omega_e > \omega_{ecmax}$, as indicated by the orange region. Let $\omega_{cn} = \omega_{cp}$ to achieve the fastest response.

By partitioning the regions, ω_{cn} can be updated in real-time according to the red curve in a lookup table for different ω_e. It should be noted that other stability indicators, such as amplitude margin or phase margin, can also be used for parameter tuning. Regardless of the indicator used, the parameter tuning regions always can be divided into three parts generally: disabling the ACRn, gradually adjusting ω_{cn}, and setting ω_{cn} equal to ω_{cp}. Different stability indicators may result in variations in the trajectory of ω_{cn} in Region II and different critical speeds of these regions, but all of them can meet the basic requirements and ensure stability.

B. Closed-Loop System and Simulations

Fig. 12 shows the overall closed-loop control diagram with the virtual-winding-based current controller, where the purple and green curves represent ACRp and ACRn, respectively. The blue region illustrates the virtual winding and VSD decoupling transformation. The red region is the proposed adaptive ω_e in Fig. 11 to ensures the stability of the closed-loop system.

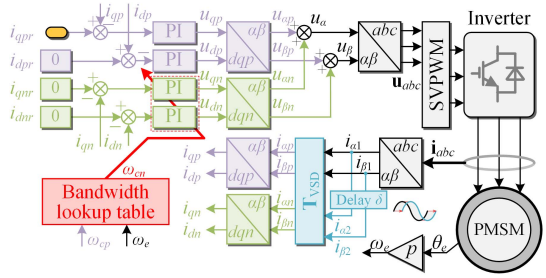

Fig. 12. Overall block diagram of the closed-loop control system with the virtual-winding-based current controller and the proposed parameter design method.

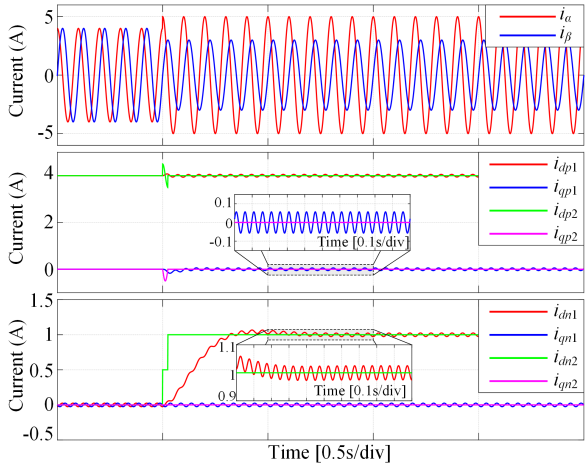

Fig. 13. Simulation results of harmonic currents extraction with LPF-based and virtual-winding-based method.

Fig. 13 presents the harmonic separation simulation results of the LPF-based algorithm proposed in [36] and the improved virtual winding-based algorithm proposed in this article. Subscripts 1 and 2 represents to the harmonics separated by the LPF and the virtual winding, respectively. At 0.5 s, $i_{dn} = 1$ A is injected into a 4 A positive-sequence current. It can be seen from Fig. 8 that the virtual winding structure completes harmonic separation rapidly within 0.5 electrical cycles. In contrast, the LPF not only exhibits slower separation but also fails to fully decouple the positive and negative sequence currents. Simulation results highlight the superior performance and fast response of the virtual winding structure.

V. Experimental Verification

To verify the proposed stability analysis results, an experimental platform was set up as shown in Fig. 14. The parameters of the tested PMSM are listed in Table I. The PMSM is driven by an SiC inverter. The dSPACE model DS1007 is used as the controller. An 18 kW power supply from iTech powers the drive system. To simulate resistance asymmetry, a 0.5 Ω resistor is connected in series with phase-A. The switching frequency is set to 10 kHz, and ω_{cp} is set to 100π. The reference values of ACRn are set to 0 A. All experimental data are exported from dSPACE and plotted using MATLAB.

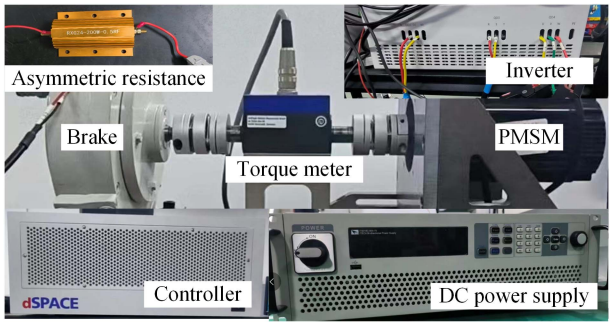

Fig. 14. Experimental setup.

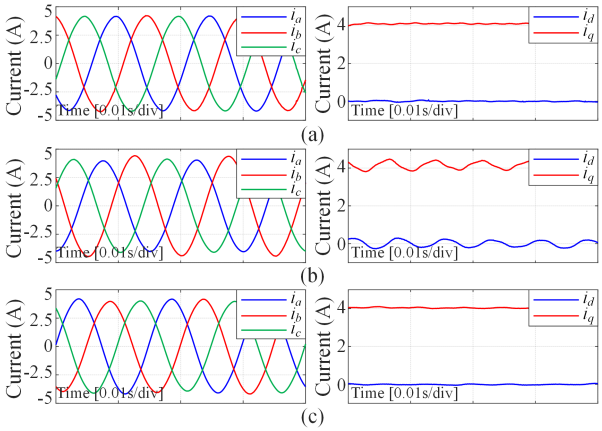

Fig. 15. Current waveforms in *abc* frame and *dq* axes. (a) Without additional resistance. (b) With additional resistance. (c) With additional resistance and negative harmonic controller by virtual winding structure.

A. Steady State Experimental Results

Fig. 15 illustrates the regulation effects of the three-phase and *dq*-axes currents under normal control, resistance asymmetry, and after adding ACRn based on the virtual winding structure. The motor operates at the rated speed of 1000 r/min with a load current of 4 A. In the normal condition shown in Fig. 15(a), the three-phase currents are nearly sinusoidal, and the *dq*-axes currents remain nearly constant. After adding a 0.5 Ω resistor in series with phase A, as shown in Fig. 15(b), obvious asymmetry appears in three phase currents, with i_d and i_q oscillation amplitudes of 0.41 and 0.52 A, respectively. After incorporating ACRn, as shown in Fig. 15(c), the current asymmetry is significantly reduced, with i_d and i_q oscillation amplitudes decreasing to 0.05 and 0.06 A, respectively, which proves the effectiveness of the virtual-winding-based current controller in steady state.

B. Dynamic State Experimental Results

Fig. 16 presents the experimental results of current and speed regulation dynamics during the activation of ACRn. The motor operates at 300 r/min, with ω_{cn} tuned as proposed in Fig. 11. ACRn is enabled at the dashed line. The negative sequence currents quickly converge to 0 A within one electrical cycle. The 2nd oscillation in mechanical speed ω_m and the i_{abc} are effectively suppressed.

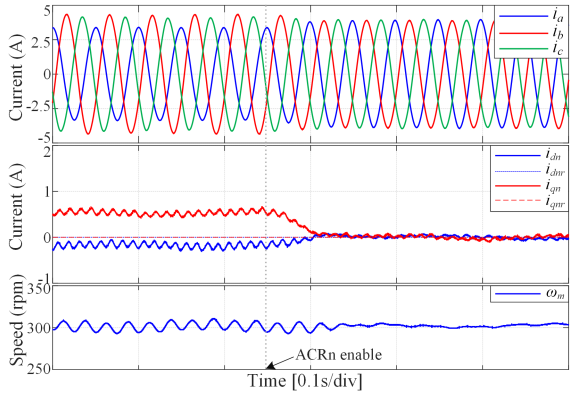

Fig. 16. Experimental results of the negative sequence currents i_{dqn}, three-phase currents i_{abc} and mechanical speed ω_m during the activation of negative sequence controller.

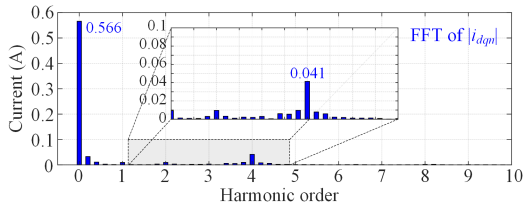

Fig. 17. FFT results of $|i_{dqn}|$ in Fig. 16 before ACRn is activated.

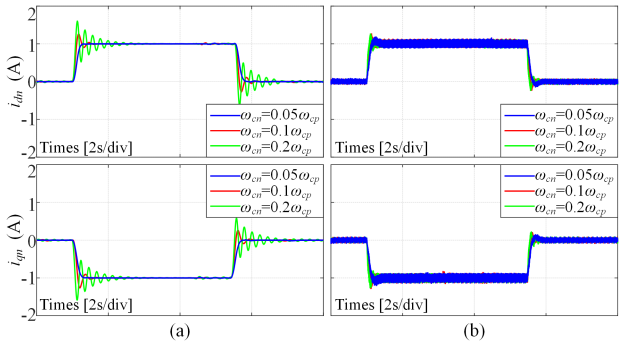

Fig. 18. Step responses of i_{dn} and i_{qn} with the LPF-based and virtual-winding based method under different ω_{cn} at 500 r/min. (a) LPF-based method. (b) Virtual-winding based method.

Fig. 17 shows the Fast Fourier Transform (FFT) results of $|i_{dqn}|$ before ACRn is activated. It can be seen from Fig. 17 that there is a small –4th disturbance in the i_{dqn}, which may result from the inverter dead-time and back EMF harmonics. This disturbance is reflected as the –4th harmonics in the *dqn* frame and –5th in the *abc* frame. Nevertheless, ACRn is still effective in regulating negative sequence harmonics.

Figs. 18 and 19 show the step response of i_{dn} and i_{qn} with the virtual-winding based and LPF-based method in [36] at 500 and 1000 r/min, respectively. The LPF bandwidths in ACRp and ACRn in the traditional method are 159.15 and 4.77 rad/s, respectively. To make a fair comparison, the same ω_{cn} are utilized, i.e., $0.05\omega_{cp}$, $0.1\omega_{cp}$, and $0.2\omega_{cp}$, respectively. The corresponding step responses are blue, red, and green curves, respectively. It can be seen from Figs. 18 and 19 that when $\omega_{cn} =$

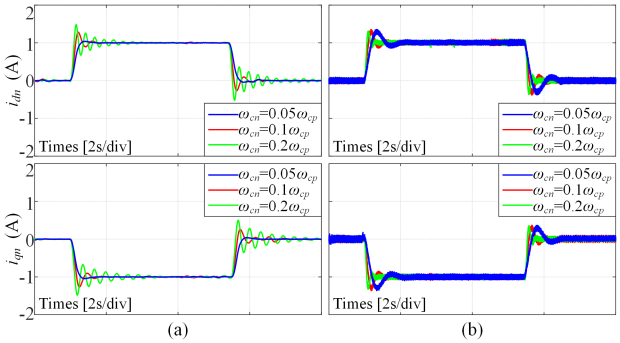

Fig. 19. Step responses of i_{dn} and i_{qn} with the LPF-based and virtual-winding based method under different ω_{cn} at 1000 r/min. (a) LPF-based method. (b) Virtual-winding based method.

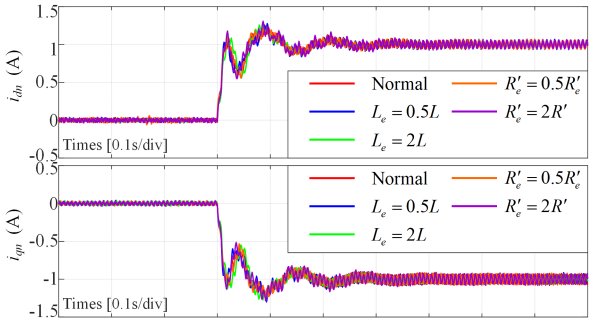

Fig. 20. Step responses of i_{dn} and i_{qn} with the virtual-winding based method under parameter mismatch.

$0.05\omega_{cp}$, the dynamic performance difference between the two methods is not obvious due to the limitation of ω_{cn}. However, when $\omega_{cn} \geq 0.1\omega_{cp}$, the traditional MSRF method shows significant oscillation due to the limitation of LPF. What is worse, when $\omega_{cn} > 0.3\omega_{cp}$, the slow dynamics of LPF even lead to instability. In contrast, the virtual-winding based method can improve the dynamic performance and ensure stability during the increasing of ω_{cn}. Therefore, compared with the traditional LPF-based method, the virtual-winding based method can achieve faster dynamic performance.

Fig. 20 shows the step response of i_{dn} and i_{qn} under estimated parameter mismatch. It can be seen from Fig. 20 that the dynamic characteristics of ACRn are almost unaffected under 0.5–2 times parameter deviation. Therefore, the virtual-winding based harmonic current controller has sufficient parameter robustness. However, the 4th harmonic fluctuation caused by the inverter dead zone still exist in the *dqn* frame. Therefore, the analysis of the harmonic controllers with multiple virtual windings is an important research direction in the future.

C. Parameterization and Stability Evaluation

Fig. 21 compares the stability using traditional fixed parameters and the proposed turning method. The motor speed gradually decreases from 450 to 320 r/min and then returns to 450 r/min. When ω_{cn} is fixed at 100π, Fig. 21(a) shows that as the speed drops below 350 r/min, the ω_m and i_{dq} begin to oscillate. As ω_m returns above 350 r/min, the oscillations gradually decrease and

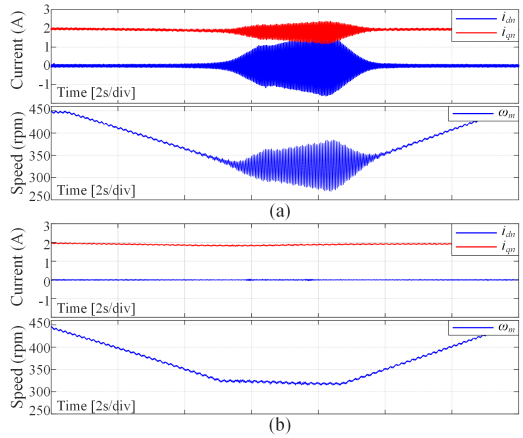

Fig. 21. Comparison of the stability of i_{dq} and ω_m during the decreasing of ω_m. (a) Traditional fixed parameter ($\omega_{cn} = \omega_{cp}$). (b) Proposed ω_{cn} designing method.

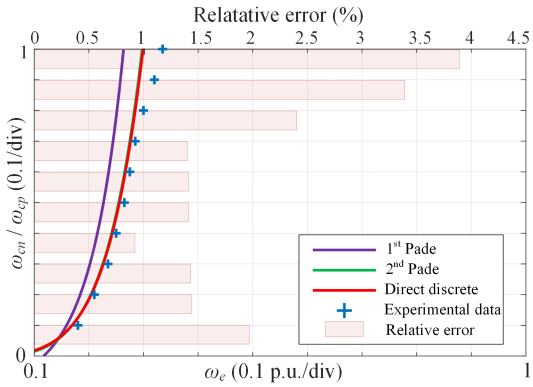

Fig. 22. Comparison of the closed-loop stability boundary between different theoretical analysis results and the experimental results.

the system stabilizes again. This proves that lower speeds can cause more instability at a fixed ω_{cn}. After using the proposed ω_{cn} tuning method, Fig. 21(b) shows that the current and speed remain stable during the speed reduction, with no oscillation. This demonstrates that the proposed tuning method can ensure stable operation of the system effectively.

Fig. 22 shows the comparison of system stability boundaries between experimental and theoretical results. The purple, green, and red curves represent the stability boundaries obtained using the 1st and 2nd Pade approximation, and direct discretization, respectively. The blue "+" symbols indicate the experimental results. Stability boundaries were tested as follows: ω_m was gradually reduced from 1000 in 5 r/min increments, and the first speed at which oscillation occurred was recorded as the instability speed. Fig. 22 shows that the 1st Pade approximation has the largest error, which may be due to the deviation of the Frequency domain characteristics. The direct discretization results are the most consistent with the experimental data. The light red bar graph shows the percentage error between the direct discretization results and the experimental results relative to the rated speed. The smallest error is 0.92% and the largest is 3.89% when $\omega_{cn} = \omega_{cp}$, which may result from deviations between the actual and estimated impedance. All errors between theory and

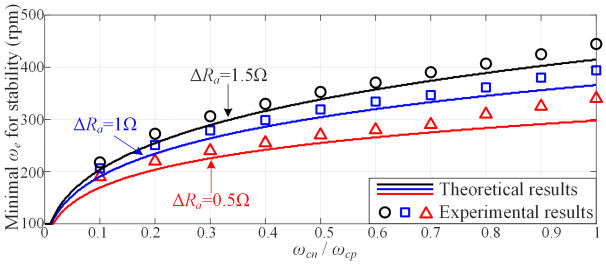

Fig. 23. Comparison of the stability boundary between different theoretical analysis results and the experimental results under different resistance asymmetries.

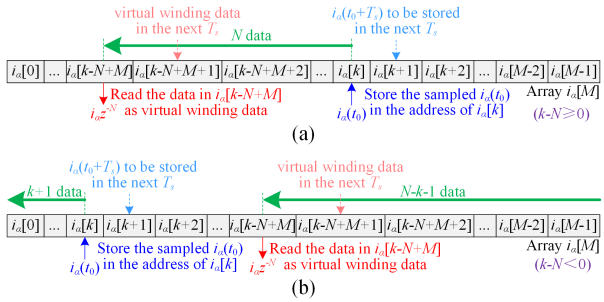

Fig. 24. Implementation of the virtual winding structure in the digital signal processors. (a) k-$N \geq 0$. (b) k-$N < 0$.

experiment are within 4%, demonstrating the accuracy of the proposed stability analysis method. Besides, it is recommended to use the 2nd or higher Pade approximation for stability analysis in future because of large computational effort required for direct discretization at low speeds.

Fig. 23 compares the experimental results and theoretical predictions of minimal critical stable speeds ω_e for different ΔR_a values. The theoretical results were derived using the 2nd Pade approximation method. As shown in Fig. 23, higher resistance deviations result in increased stability boundaries under the same ω_{cn}, and the stability range becomes narrower. The theoretical predictions closely align with the experimental data, with a maximum error of less than 4%, which verifies the effectiveness of the proposed stability analysis method under different resistance asymmetries.

D. Implementation and Execution Time in MCU

Fig. 24 illustrates the implementation of the virtual winding algorithm in DSP TMS320F28377D. For the variable i_α, an array $i_\alpha[M]$ is used to store past sample values, where M denotes the maximum number of sampling points. The sampled i_α is stored at position $i_\alpha[k]$, and N previous sampling data are retrieved as the virtual winding current of i_α. If k-$N \leq M$, the retrieval wraps around to the end of the array, as shown in Fig. 24(b). A similar approach can be used to construct the virtual winding for i_β.

To evaluate the computational burden of the proposed method, the execution time with the LPF-based harmonic controller in [36], the traditional virtual winding method in [24], and the proposed method with ω_{cn} lookup table is compared. The results

TABLE II
COMPARISON OF EXECUTION TIME OF DIFFERENT METHODS

Method	Execution time (μs)		
	Sin, Cos	+ - * /	Total
Method in [36]	4.42	1.20	5.62
Method in [24]	4.42	2.43	6.85
Proposed method	4.42	2.94	7.36

are presented in Table II. As shown in Table II, the execution time of the proposed method increases slightly, but remains within acceptable limits for a controller operating at 10 kHz.

VI. CONCLUSION

This article reveals the equivalent transfer function model of the virtual winding structure for the first time. Stability conditions for the closed-loop system are derived in both the continuous and discrete domains. Pade approximation is used to transform the transcendental equation into a polynomial equation. The main contributions of this article are as follows.

1) The discretized closed-loop system is a variable-order system dependent on speed. Direct discretization analysis is accurate but becomes increasingly complex as rotational speed decreases and the system's equivalent order increases.
2) The order of the Pade approximation affects the accuracy of stability analysis. To balance accuracy and computational efficiency, the 2nd Pade approximation is recommended.
3) Based on the analyzed stability region, a parameter tuning method is provided to achieve the fastest dynamics while ensuring system stability.
4) The stability boundaries obtained from theoretical analysis and experimental validation are consistent, with a maximum error not exceeding 4%, demonstrating the accuracy of the proposed method.

However, there are several limitations in this study. For IPMSMs with saliency, the analysis method based on complex vectors is not applicable. Instead, the analysis method of MIMO systems is required. Additionally, to mitigate errors caused by the inverter's dead time and back-EMF harmonics, additional –6th harmonic controller should be incorporated. The stability analysis with multiple virtual windings is the focus of future work.

APPENDIX

The coefficients of (17) can be expressed as follows:

$$\begin{cases} a_3 = 2L \\ a_2 = 2R' + L\left(\left(1 - je^{-s\delta}\right)\omega_{cn} + \left(1 + je^{-s\delta}\right) \times \omega_{cp}\left(e^{-s\delta} - j\right)\omega_e\right) \\ a_1 = R'\left(\left(1 - je^{-s\delta}\right)\omega_{cn} + \left(1 + je^{-s\delta}\right)\omega_{cp}\right) + 2L{\omega_e}^2 \\ a_0 = \omega_e R'\left(\left(j - e^{-s\delta}\right)\omega_{cp} - \left(j + e^{-s\delta}\right)\omega_{cn} + 2\omega_e\right) + {\omega_e}^2 L\left(\left(1 - je^{-s\delta}\right)\omega_{cn} + \left(1 + je^{-s\delta}\right) \times \omega_{cp}\left(e^{-s\delta} - j\right)\omega_e\right). \end{cases} \tag{26}$$

The coefficients of (22) can be expressed as follows:

$$b_5 = L\pi^2 \tag{27}$$

$$b_4 = \pi^2 R' + 8L\pi\omega_e \tag{28}$$

$$b_3 = 2\omega_e \left(4\pi R' + 2L\pi \left(\omega_{cn}+\omega_{cp} - j\omega_e\right) + 8L\omega_e + L\pi^2\omega_e\right) \tag{29}$$

$$b_2 = 2\omega_e \begin{pmatrix} \pi^2 R'\omega_e + 8\left(R' + L\left(\omega_{cn} + \omega_{cp} - j\omega_e\right)\right)\omega_e \\ +2\pi\left(R'\left(\omega_{cn} + \omega_{cp}\right) + L\omega_e\left(-j\omega_{cn} + j\omega_{cp} + 3\omega_e\right)\right) \end{pmatrix} \tag{30}$$

$$b_1 = {\omega_e}^2 \begin{pmatrix} 8R'\left(\left(2 - j\pi\right)\omega_{cn} + \left(2 + j\pi\right)\omega_{cp} + \pi\omega_e\right) \\ +L\omega_e\left(4\pi\left(\omega_{cn} + \omega_{cp}\right) + \left(16 + \pi\left(-4j + \pi\right)\right)\omega_e\right) \end{pmatrix} \tag{31}$$

$$b_0 = {\omega_e}^3 \begin{pmatrix} -4R'\left(\left(4j + \pi\right)\omega_{cn} + \left(-4j + \pi\right)\omega_{cp}\right) + \left(16 + \pi^2\right)R'\omega_e \\ +4L\omega_e\left(\left(4 - j\pi\right)\omega_{cn} + \left(-4j + \pi\right)\left(j\omega_{cp} + \omega_e\right)\right) \end{pmatrix}. \tag{32}$$

REFERENCES

[1] T. Wang, L. Guo, K. Wang, J. Wu, C. Liu, and Z. Zhu, "Generalized predictive current control for dual-three-phase PMSM to achieve torque enhancement through harmonic injection," *IEEE Trans. Power Electron.*, vol. 38, no. 5, pp. 6422–6433, May 2023.

[2] T. Zhao, S. Wu, and S. Cui, "Multiphase PMSM with asymmetric windings for more electric aircraft," *IEEE Trans. Transp. Electrific.*, vol. 6, no. 4, pp. 1592–1602, Dec. 2020.

[3] S. Sonandkar, R. Selvaraj, and T. R. Chelliah, "Fault tolerant capability of battery assisted quasi-z-source inverter fed five phase PMSM drive for marine propulsion applications," in *Proc. IEEE Int. Conf. Power Electron., Drives Energy Syst.*, 2020, pp. 1–6.

[4] D. Zhang et al., "A PMSM control system for electric vehicle using improved exponential reaching law and proportional resonance theory," *IEEE Trans. Veh. Technol.*, vol. 72, no. 7, pp. 8566–8578, Jul. 2023.

[5] L. Wu and Z. Lyu, "Harmonic injection-based torque ripple reduction of PMSM with improved DC-Link voltage utilization," *IEEE Trans. Power Electron.*, vol. 38, no. 7, pp. 7976–7981, Jul. 2023.

[6] H. Lin, Y. Liao, L. Yan, F. Li, and Y. Feng, "A novel modulation-based current harmonic control strategy for PMSM considering current measurement error and asymmetric impedance," *IEEE Access*, vol. 10, pp. 89346–89357, 2022.

[7] M. Hu, W. Hua, Z. Wu, N. Dai, H. Xiao, and W. Wang, "Compensation of current measurement offset error for permanent magnet synchronous machines," *IEEE Trans. Power Electron.*, vol. 35, no. 10, pp. 11119–11128, Oct. 2020.

[8] T. Qiu, X. Wen, and F. Zhao, "Adaptive-linear-neuron-based dead-time effects compensation scheme for PMSM drives," *IEEE Trans. Power Electron.*, vol. 31, no. 3, pp. 2530–2538, Mar. 2016.

[9] X. Liu, D. Liang, J. Du, Y. Yu, X. Yang, and Z. Luo, "Effects analysis of misalignments on dynamic characteristics test for permanent magnet synchronous motor," in *Proc. 17th Int. Conf. Elect. Mach. Syst.*, 2014, pp. 1543–1547.

[10] X. Sun, M. Wu, G. Lei, Y. Guo, and J. Zhu, "An improved model predictive current control for PMSM drives based on current track circle," *IEEE Trans. Ind. Electron.*, vol. 68, no. 5, pp. 3782–3793, May 2021.

[11] W. Xu, S. Qu, and C. Zhang, "Fast terminal sliding mode current control with adaptive extended state disturbance observer for PMSM system," *IEEE J. Emerg. Sel. Topics Power Electron.*, vol. 11, no. 1, pp. 418–431, Feb. 2023.

[12] W. Wang, C. Liu, Z. Song, and Z. Dong, "Harmonic current suppression for dual three-phase PMSM based on deadbeat control and disturbance observer," *IEEE Trans. Ind. Electron.*, vol. 70, no. 4, pp. 3482–3492, Apr. 2023.

[13] F. Wang, W. Kong, and R. Qu, "Model parameter self-correcting deadbeat predictive current control for SPMSM drives," *IEEE Trans. Ind. Electron.*, early access, Aug. 19, 2024, doi: 10.1109/TIE.2024.3436609.

[14] P. Xia, W. Li, Y. Cui, Y. Zhu, and L. Guo, "Repetitive disturbance observer based composite current control for PMSM with harmonic reducer," *IEEE Trans. Ind. Electron.*, early access, Sep. 5, 2024, doi: 10.1109/TIE.2024.3443957.

[15] Z. Lyu and L. Wu, "Resonant frequency deviation analysis and modified notch filter-based active damping for SiC-Based PMSM drive with sine wave filter," *IEEE Trans. Energy Convers.*, vol. 38, no. 1, pp. 417–427, Mar. 2023.

[16] B. Liu, B. Zhou, and T. Ni, "Principle and stability analysis of an improved self-sensing control strategy for surface-mounted PMSM drives using second-order generalized integrators," *IEEE Trans. Energy Convers.*, vol. 33, no. 1, pp. 126–136, Mar. 2018.

[17] Y. Sun, M. Yang, B. Wang, Y. Chen, and D. Xu, "Precise position control based on resonant controller and second-order sliding mode observer for PMSM-driven feed servo system," *IEEE Trans. Transp. Electrific.*, vol. 9, no. 1, pp. 196–209, Mar. 2023.

[18] X. Liu, Y. Deng, J. Wang, H. Li, and H. Cao, "Fixed-time generalized active disturbance rejection with quasi-resonant control for PMSM speed disturbances suppression," *IEEE Trans. Power Electron.*, vol. 39, no. 6, pp. 6903–6918, Jun. 2024.

[19] B. Wang, M. Tian, Y. Yu, Q. Dong, and D. Xu, "Enhanced ADRC with quasi-resonant control for PMSM speed regulation considering aperiodic and periodic disturbances," *IEEE Trans. Transp. Electrific.*, vol. 8, no. 3, pp. 3568–3577, Sep. 2022.

[20] P. L. Chapman and S. D. Sudhoff, "A multiple reference frame synchronous estimator/regulator," *IEEE Trans. Energy Convers.*, vol. 15, no. 2, pp. 197–202, Jun. 2000.

[21] H. Zhang, M. Dou, and J. Deng, "Loss-minimization strategy of nonsinusoidal back EMF PMSM in multiple synchronous reference frames," *IEEE Trans. Power Electron.*, vol. 35, no. 8, pp. 8335–8346, Aug. 2020.

[22] E. Uz-Logoglu, O. Salor, and M. Ermis, "Online characterization of interharmonics and harmonics of AC electric arc furnaces by multiple synchronous reference frame analysis," *IEEE Trans. Ind. Appl.*, vol. 52, no. 3, pp. 2673–2683, May 2016.

[23] L. Yan et al., "Multiple synchronous reference frame current harmonic regulation of dual three phase PMSM with enhanced dynamic performance and system stability," *IEEE Trans. Ind. Electron.*, vol. 69, no. 9, pp. 8825–8838, Sep. 2022.

[24] L. Yan et al., "Suppression of major current harmonics for dual three-phase PMSMs by virtual multi three-phase systems," *IEEE Trans. Ind. Electron.*, vol. 69, no. 6, pp. 5478–5490, Jun. 2022.

[25] Z. Lyu, L. Wu, J. Yi, and S. Yang, "Hybrid frame-based current control scheme for LC-equipped PMSM with non-sinusoidal back-EMF," *IEEE Trans. Power Electron.*, vol. 38, no. 5, pp. 5994–6004, May 2023.

[26] L. Yan et al., "Arbitrary current harmonic decomposition and regulation for permanent magnet synchronous machines," *IEEE Trans. Ind. Electron.*, vol. 70, no. 5, pp. 4392–4404, May 2023.

[27] S. K. Kommuri, Y. Park, and S. B. Lee, "High-resistance fault control in permanent magnet synchronous motors," *IEEE/ASME Trans. Mechatronics*, vol. 25, no. 1, pp. 271–281, Feb. 2020.

[28] K. Thapa, P. Korta, M. S. Toulabi, L. V. Iyer, and N. C. Kar, "Torque ripple reduction in a traction IPMSM with resistance asymmetry using an adaptive PIR current controller," in *Proc. IEEE 1st Ind. Electron. Soc. Annu. Line Conf.*, 2022, pp. 1–6.

[29] N. Nakao and K. Akatsu, "Suppressing pulsating torques: Torque ripple control for synchronous motors," *IEEE Ind. Appl. Mag.*, vol. 20, no. 6, pp. 33–44, Nov. 2014.

[30] F. Briz, M. W. Degner, and R. D. Lorenz, "Analysis and design of current regulators using complex vectors," *IEEE Trans. Ind. Appl.*, vol. 36, no. 3, pp. 817–825, May/Jun. 2000.

[31] C. Glader, G. Högnäs, P. Mäkilä, and H. Toivonen, "Approximation of delay systems—A case study," *Int. J. Control*, vol. 53, no. 2, pp. 369–390, 1991.

[32] M. Hu et al., "Fast current control without computational delay by minimizing update latency," *IEEE Trans. Power Electron.*, vol. 36, no. 11, pp. 12207–12212, Nov. 2021.

[33] L. Zhu, L. Wu, J. Liu, and Y. Guo, "Negative sequence current suppression of dual three-phase permanent magnet synchronous machines considering inductance asymmetry," in *Proc. 22nd Int. Conf. Elect. Mach. Syst.*, 2019, pp. 1–6, doi: 10.1109/ICEMS.2019.8921574.

[34] M. Xu, L. Wu, X. Huang, Y. Fang, and J. Liu, "Improved sensorless control for permanent-magnet synchronous motor with self-inductance asymmetry," in *Proc. IEEE Int. Elect. Mach. Drives Conf.*, 2019, pp. 939–944, doi: 10.1109/IEMDC.2019.8785342.

[35] L. Wu, Z. Lyu, Z. Chen, J. Liu, and Y. Lu, "An enhanced sensorless control scheme for PMSM drives considering self-inductance asymmetry," *CES Trans. Elect. Mach. Syst.*, vol. 6, no. 4, pp. 384–392, Dec. 2022, doi: 10.30941/CESTEMS.2022.00050.

[36] J. Karttunen, S. Kallio, J. Honkanen, P. Peltoniemi, and P. Silventoinen, "Partial current harmonic compensation in dual three-phase PMSMs considering the limited available voltage," *IEEE Trans. Ind. Electron.*, vol. 64, no. 2, pp. 1038–1048, Feb. 2017.

[37] S. Skogestad and I. Postlethwaite, *Multivariable Feedback Control: Analysis and Design*, 2nd ed. Hoboken, NJ, USA: Wiley, 2005.

Pingyue Song (Student Member, IEEE) received the B.Eng. degree in electrical engineering from the Hebei University of Technology, Tianjin, China, in 2021. He is currently working toward the Ph.D. degree in electrical engineering with Zhejiang University, Hangzhou, China.

His current research interests include control of motor drive systems and sensor error compensation.

Lijian Wu (Senior Member, IEEE) received the B.Eng. and M.Sc. degrees from Hefei University of Technology, Hefei, China, in 2001 and 2004, respectively, and the Ph.D. degree from the University of Sheffield, Sheffield, U.K., in 2011, all in electrical engineering.

From 2004 to 2007, he was an Engineer with Delta Electronics (Shanghai) Co. Ltd. From 2012 to 2013, he was with Sheffield Siemens Wind Power Research Center as a design Engineer focusing on wind power generators. From 2013 to 2016, he was an advanced Engineer with Siemens Wind Power A/S, Brande, Denmark. Since 2016, he has been with Zhejiang University, Hangzhou, China, where he is currently a Professor of electrical machines and control systems. His current major research interests include design and control of permanent magnet machines.

Tao Wang (Senior Member, IEEE) received the B.Eng. and Ph.D. degrees in electrical engineering from the College of Electrical Engineering, Zhejiang University, Hangzhou, China, in 2013 and 2018, respectively.

From 2018 to 2020, he worked as a Postdoc Research Associate with the Department of Electronic and Electrical Engineering, University of Sheffield, U.K. From 2020 to 2023, he was with the Nanjing University of Aeronautics and Astronautics, Nanjing, China, where he worked as an Associate Professor in the College of Automation Engineering. Since 2024, he has been a Research Professor with the College of Electrical Engineering, Zhejiang University. His current research interests include wind power generation, aviation power supply, permanent magnet synchronous machine control, and model predictive control.